

An investigation on the role of W doping in BiVO₄ photoanodes used for solar water splitting

Zhao, Xin; Hu, Jun; Chen, Shi; Chen, Zhong

2018

Zhao, X., Hu, J., Chen, S., & Chen, Z. (2018). An investigation on the role of W doping in BiVO₄ photoanodes used for solar water splitting. *Physical Chemistry Chemical Physics*, 20(19), 13637-13645. doi:10.1039/C8CP01316K

<https://hdl.handle.net/10356/106075>

<https://doi.org/10.1039/C8CP01316K>

© 2018 Owner Societies. All rights reserved. This paper was published in *Physical Chemistry Chemical Physics* and is made available with permission of Owner Societies.

Downloaded on 13 Mar 2024 14:45:43 SGT

An investigation on the role of W doping in BiVO₄ photoanodes used for solar water splitting

Xin Zhao,^{‡a} Jun Hu,^{‡*a, c} Shi Chen,^b and Zhong Chen^{*a}

a. School of Materials Science and Engineering, Nanyang Technological University, 50 Nanyang Avenue, 639798, Singapore, Singapore.

b. School of Physical and Mathematical Sciences, Nanyang Technological University, 637371, Singapore, Singapore

c. School of Chemical Engineering, Northwest University, Xi'an, P. R. China 710069

E-mail: hujun@nwu.edu.cn; ASZChen@ntu.edu.sg

Abstract

N-type doping has been widely employed to enhance the performance of photoanode in a photoelectrochemical cell for water splitting. However, little is known about how the doping affects the catalytic activity on the surface. Herein, we take BiVO₄ as an example to investigate effect of doping on surface catalysis from both experimental and theoretical perspectives. To enable impartial comparison, we have prepared planar BiVO₄ thin films with and without W doping. The W doping has no obvious effect on the film morphology, crystallinity and light absorption, however, the photocurrent is significantly enhanced by W doping. Such enhancement is contributed by two important factors, i.e., a better charge separation efficiency and an improved surface charge transfer efficiency. Electrochemical analysis reveals that W doping lowers the surface charge transfer resistance and forms active surface states facilitating the charge transfer. Theoretical analysis shows that W doping activates V atoms into reactive sites. Meanwhile, the adsorption energies and distance of the adsorption species, OH_{ads}, O_{ads} and OOH_{ads} involved in the water splitting process become more favorable for the surface charge transfer. The current study provides insights into the roles of doping in BiVO₄, especially on the surface catalysis.

Key word: Photoelectrochemical water splitting; BiVO₄; W doping; Surface catalysis; Charge transfer; First principles calculation.

1. Introduction

Photoelectrochemical (PEC) water splitting is a promising route to generate hydrogen fuel to solve energy and environmental issues by converting and storing intermittent and inexhaustible solar energy into chemical bonds.¹⁻³ Compared with photocathode semiconductor for hydrogen evolution, the low efficiency in oxygen evolving reaction in the photoanode poses a greater challenge in order to achieve a highly efficient overall water splitting.⁴ As a result, a great deal of attention has been paid on improving the performance of photoanode. Monoclinic scheelite bismuth vanadate (BiVO_4) has recently been identified as one of the most promising photoanode materials for PEC water splitting.^{2, 5-17} The theoretical solar to hydrogen conversion efficiency is about 9.1% with the band gap of 2.4 eV. Moreover, this material has favorable band edge positions, with the conduction band minimum close to H_2O reduction potential and a more positive potential of the valence band maximum than the H_2O oxidation potential. As a result, it shows a good onset potential for water oxidation among most visible light responsive photoanodes.

The solar energy conversion efficiency of BiVO_4 for water splitting is determined by 3 factors, *viz.*, solar light absorption efficiency, charge separation efficiency in the bulk of the photoelectrode, and interfacial charge transfer efficiency at the electrode/electrolyte junction. Light absorption efficiency is affected by 2 factors: the band gap of the semiconductor material and its interaction with incoming photons. The second factor depends on, and thus is controllable by tuning the surface nanostructures and the thickness in order to enhance the light absorption. After the capture of light, electrons and holes are generated and ideally, the charges are separated towards the cathode and anode. The charge separation efficiency determines how many photo-generated carriers have successfully transported to the surfaces of the electrodes. Finally, the carriers that have reached the surface, they will either react with water to generate O_2 and H_2 , or recombine to generate heat. It is difficult to change the bandgap of BiVO_4 , therefore enhancing the charge separation and avoiding surface recombination are feasible solutions. To avoid recombination at the

electrode surface, the surface states play a very important role.¹⁸ In the past, many studies have been devoted to the use of co-catalysts (or electrocatalysts) to suppress the recombination, and great amount progress has been achieved.^{11, 19-21} For the charge separation, it has been well understood that it is affected by several factors, such as lattice scattering, defects trapping, grain boundary recombination. Usually, for a photoanode such as BiVO₄, poor electron conductivity is a critical factor, which limits the charge transport. Doping has been widely employed to improve the performance. For example, W or Mo doping is normally taken to improve the conductivity of BiVO₄ photoanode.^{6, 8, 11, 13, 15, 22} The most accepted reason for the observed enhancement is the improved electron conductivity caused by n-type doping to increase electron density of BiVO₄. However, surface issue, such as surface states, is also an important point to consider as discussed above. Doping can also potentially cause change in the surface condition, which has not received much attention so far. Therefore a comprehensive approach is needed to investigate both bulk charge separation and surface charge transport, with a particular focus on how the surface chemistry has changed due to doping.

In this study, we fabricated BiVO₄ thin films with or without W doping by a drop-casting method reported in a previous work.²³ We used a planar dense structure in this study to minimize the interference caused by the nanostructure on the light absorption, which makes the study focused on the mechanisms behind the doping effect. The effect of W doping into BiVO₄ was discussed from both experimental and theoretical perspectives. It was found that W doping changes the active sites and adsorption of water on the surface of BiVO₄, which have greatly enhanced the surface charge transfer.

2. Methods and characterization

2.1 Preparation of W-doped BiVO₄ thin films

Pristine and W-doped BiVO₄ thin films were fabricated by the drop-casting method reported before.²³ Bismuth trioxide, ammonium metavanadate, and ammonium tungstate hydrate were dissolved in ethylene

glycol with proper amount of nitric acid to form 0.1 M Bi, V and W aqueous precursor solutions respectively. The solutions were mixed well according to stoichiometric ratio of Bi:V=1:1 for pristine BiVO₄ (PBVO), and Bi:V:W=100:97:3 for W-doped BiVO₄ (WBVO). The corresponding volume ratio is 500 μ l : 500 μ l for PBVO, and 500 μ l : 485 μ l : 15 μ l for WBVO. Citric acid (CA) was added according to stoichiometric ratio of CA:M=1.5:1 (M is the total amount of cation). The mixture was then added with 2 ml ethylene glycol. After mixing, 60 μ l of the precursor solution was drop cast onto the exposed half side of a 1 cm \times 2 cm FTO substrates with the other half covered by a thermal tape. The samples were then dried at 120°C for 30 minutes to obtain the gel films. After peeling off the covered thermal tape, samples were subsequently put into a furnace for heat treatment at 500 °C for 2 h in air. The ramping rate at set at 10 °C/min.

2.2 Characterization

Crystallinity of PBVO and WBVO thin films were identified by X-ray diffraction (XRD, Shimadzu 6000 X-ray diffractometer) with Cu K α radiation (λ = 0.154 nm). The morphologies of PBVO and WBVO thin films were observed using field emission scanning electron microscopy (FESEM, JEOL JSM-7600F). The light absorption efficiency of PBVO and WBVO thin films was determined based on the reflectance and transmittance spectra using a UV-Vis-NIR spectrophotometer (Lambda 950, Perkin-Elmer) with an integrating sphere. The chemical state of W was investigated by X-ray photoelectron spectroscopy (XPS, Omicron EA125). The binding energy was calibrated by C1s (284.6 eV). PEC measurement of PBVO and WBVO thin films was carried out using a three electrode configuration (PCI4/300™ potentiostat with PHE200™ software, Gamry Electronic Instruments, Inc.), with PBVO or WBVO thin films as the working electrodes, Pt mesh as the counter electrode and Ag/AgCl as the reference electrode. A solar simulator (HAL-320, Asahi Spectra Co., Ltd.) with power intensity of 100 mW·cm⁻² calibrated by a solar reference cell was used as light source for the PEC measurement. The photocurrent for water oxidation was measured in 0.5 M Na₂SO₄ aqueous solution with a scan rate of 30 mV·s⁻¹. The photocurrent was also measure with hole scavenger, 0.5 M Na₂SO₄ aqueous solution mixed with 0.1 M Na₂SO₃, added for

the evaluation of charge separation efficiency and charge transfer efficiency. Electrochemical impedance spectroscopy (EIS) measurement was carried out under AM 1.5G solar simulator illumination in 0.5 M Na_2SO_4 electrolyte at the applied potential of 1.23 V vs. RHE using an AUTOLAB Potentiostat-Galvanostat (AUTOLAB PGSTAT302 N). The Mott-Schottky plot was made using the same AUTOLAB Potentiostat-Galvanostat at a fixed frequency of 1 kHz in 0.5 M Na_2SO_4 solution in the dark.

2.3 Calculation methods

The CASTEP module of the Materials Studio software (Accelrys Inc.) was employed for the quantum chemistry calculations. During the calculations, the $2 \times 1 \times 2$ BiVO_4 (space group 15) structure with crystallographic parameters of $14.602 \text{ \AA} \times 11.704 \text{ \AA} \times 10.290 \text{ \AA}$ was used for bulk property calculation. For the doped case, one V atom is replaced by W atom to represent the W doped BiVO_4 . A 2×2 supercell of W doped BiVO_4 (010) surface with a vacuum region of 15 \AA was chosen to investigate the surface property. The (010) surface was used because it is the most stable surface under the realistic conditions.^{13, 24, 25} During the calculation, self-consistent periodic Density Functional Theory (DFT) calculations were employed. The Generalized Gradient Approximation (GGA), in the form of the Perdew-Burke-Ernzerhof (PBE) approximation was used to calculate the exchange-correlation energy. The Broyden-Fletcher-Goldfarb-Shanno (BFGS) scheme was chosen as the minimization algorithm. DFT-D correction was applied during the dispersion corrections. Hubbard U-corrections to the d electrons of V (LDA+U, effective $U(\text{V})=2.5 \text{ eV}$) and spin-polarization were performed during the calculations. Ultrasoft pseudopotentials in reciprocal space were used, where the electron configuration of the valence was set as $\text{O}-2s^2 2p^4$, $\text{Ti}-3s^2 3p^6 3d^2 4s^2$, $\text{V}-3p^6 3d^3 4s^2$, $\text{W}-5p^6 5d^4 6s^2$, and $\text{Bi}-5d^{10} 6s^2 6p^3$. Gaussian smearing scheme with the smearing width of 0.05 eV with 30% empty band was applied in the calculation. The external stress and hydrostatic pressure were set at 0 GPa. The energy cutoff was set at 380 eV and the SCF tolerance $1.0 \times 10^{-6} \text{ eV/atom}$. **The convergence criteria for the structure optimization and energy calculation were set to an energy tolerance of $5.0 \times 10^{-6} \text{ eV/atom}$, a maximum force tolerance of 0.01 eV/ \AA , 0.02 GPa and a maximum displacement tolerance of $5.0 \times 10^{-4} \text{ \AA}$, respectively.** $2 \times 2 \times 3$ k-points sampling was used for the

bulk and $2 \times 1 \times 1$ for the surface calculations. The Fermi level is simply defined as the valence band maximum (VBM) for n-type semiconductors and insulators in the CASTEP code and some other codes.^{26,}

²⁷ More calculation details are given in the supporting information.

3. Results and discussion

3.1 Experimental results

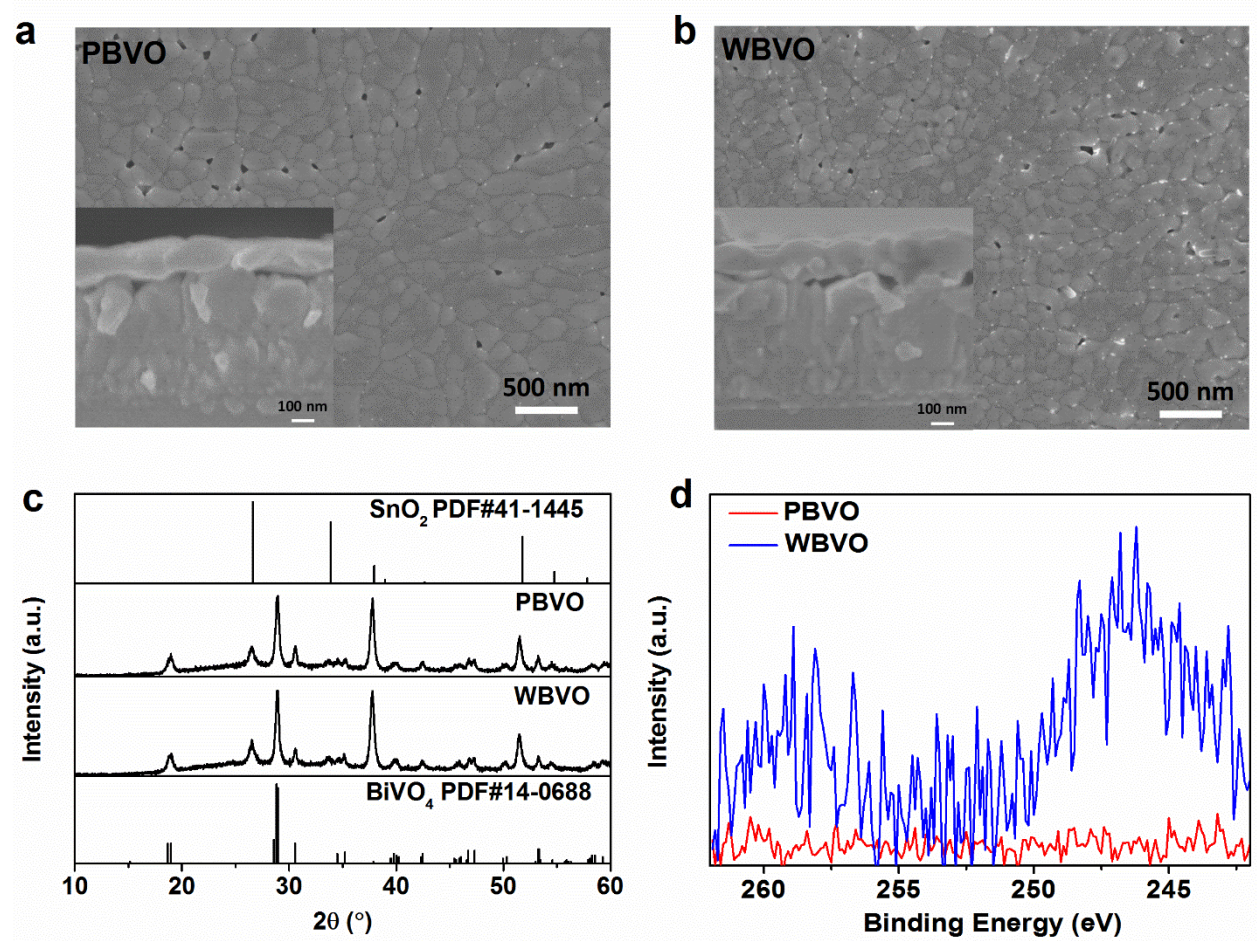


Fig. 1 SEM images of (a) PBVO and (b) WBVO. (c) X-ray diffraction of PBVO and WBVO. (d) W 4d XPS spectroscopic spectra of PBVO and WBVO.

Fig. 1a-b illustrates the morphologies of PBVO and WBVO. Both samples display very similar surface morphology of a dense film with small particle nodules. The film thickness is 162 nm and 154 nm for

PBVO and WBVO, respectively (insets in Fig. 1a and 1b) X-ray diffraction (Fig. 1c) shows all peaks of PBVO and WBVO thin films agree well with the one of BiVO_4 (PDF#14-0688), and no peaks belonging to other phases are present except the ones from the substrate FTO (SnO_2). These results demonstrate that W doping has no obvious changes on the morphology and crystallinity of BiVO_4 . The chemical states of W are investigated by XPS, and the spectra for W 4d are shown in Fig. 1d. Compared with PBVO, two peaks from W 4d are observed, which indicates that W has been successfully incorporated into BiVO_4 . The W was ~ 1.8 wt% or 0.58 at% based on EDX estimation (Table S1). The corresponding W doping level is W : Bi = 3.1 : 100, close to the experimental ratio of 3 : 100.

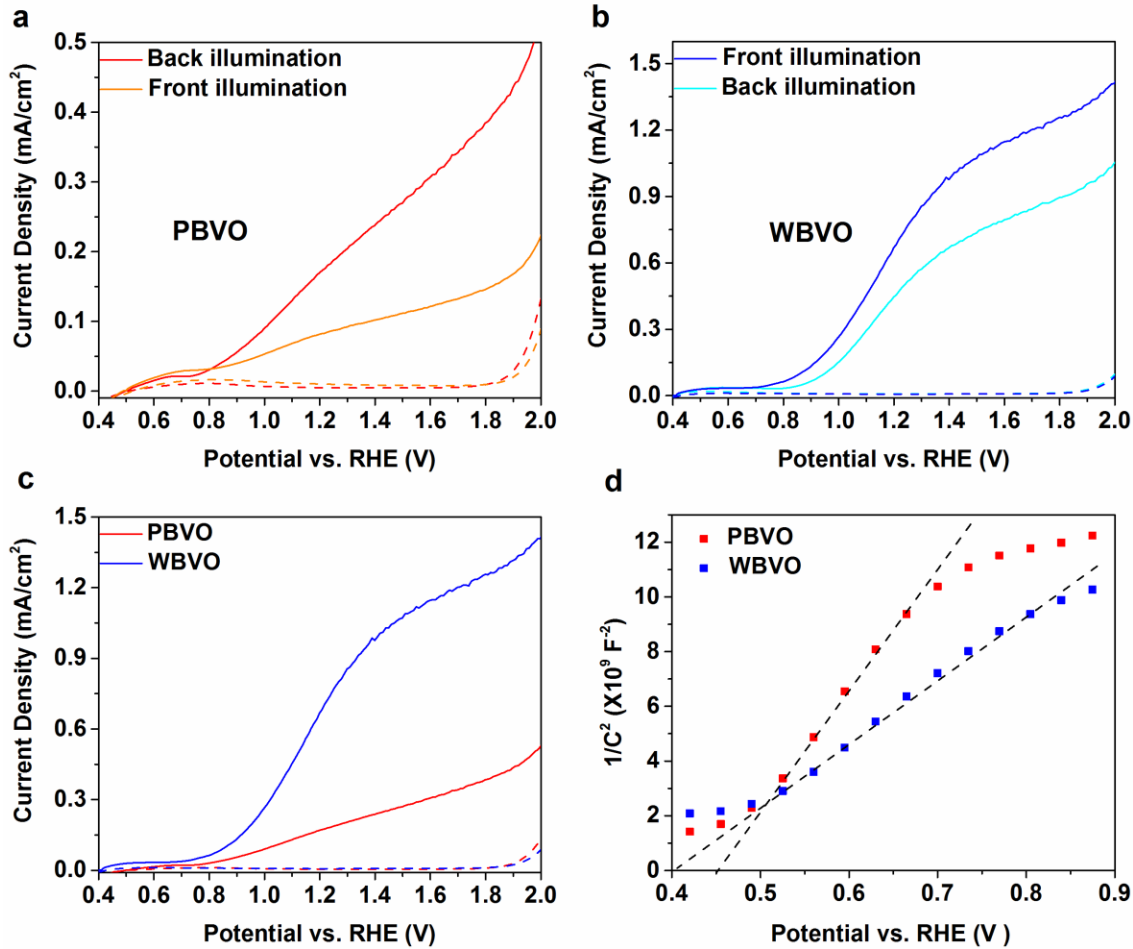


Fig. 2 Front (from liquid/sample side) and back side (from substrate/sample side) illumination photocurrents of (a) PBVO and (b) WBVO thin films. (c) Comparison of the best photocurrents of

PBVO (back side illumination) and WBVO (front side illumination). (d) Mott-Schottky plots of PBVO and WBVO measured at a fixed frequency of 1 kHz in 0.5M Na₂SO₄ aqueous solution in the dark.

Fig. 2 shows the photocurrents of PBVO and WBVO thin films from front (from the liquid/sample side) and back side (from substrate/sample side) illumination. For front side illumination, the photo-excited carriers are generated mostly near the liquid/sample interface region. Thus, when illuminated from the front side, the electron has to transport a relatively long way to conductive substrate, while the hole travels a short distance to the liquid. On the contrary, for the back side illumination, the photo-excited carriers are mostly generated near the FTO-BiVO₄ interface region. Thus, when illuminated from the back side, the hole has to travel a relatively long path to the liquid, while the electron will transport a relatively short distance to the conductive substrate. Hence, comparison of photocurrents from front and back illumination can reflect the relative transport property of electrons and holes. Fig. 2a shows that the back side illumination photocurrent is higher than that of front side illumination, which indicates the poor electron transport property of PBVO. However, for the W doped sample, the front side illumination photocurrent is higher than that of back side illumination (Fig. 2b), which indicates a much better electron transport in WBVO. Based on the observations, W doping have greatly enhanced the photocurrent (Fig. 2c), and this improvement is attributed to the much improved electron transport by increasing the electron density through W doping. The photocurrent of PBVO at 1.23 V vs. RHE is around 0.18 mA/cm², while that of WBVO has been increased by ~300% to 0.74 mA/cm². To confirm that the enhanced performance is contributed by the improved electron conductivity, Mott-Schottky plots of PBVO and WBVO (Fig. 2d) are obtained to calculate the carrier density. The majority carrier (electron) density is estimated by:

$$N_d = \frac{2}{A^2 e_0 \epsilon \epsilon_0} \left[d \left(\frac{1}{C^2} \right) / dV \right]^{-1} \quad (1)$$

where A is electrode area (1 cm² in this study), e_0 is the electron charge (1.60×10^{-19} C), ϵ is the dielectric constant of BiVO₄ (68), ϵ_0 is the permittivity of vacuum (8.85×10^{-12} F·m⁻¹), N_d is the donor density and V is the potential applied at the electrode. The slope of sample WBVO is lower than PBVO, which indicates

a higher carrier density in WBVO. The estimated electron density of PBVO is $2.9 \times 10^{20} \text{ cm}^{-3}$ according to equation (1), and this relatively high level is owing to the n-type nature of PBVO. After doping, the electron density of WBVO increased to $5.8 \times 10^{20} \text{ cm}^{-3}$. The net increase in the density, $2.9 \times 10^{20} \text{ cm}^{-3}$, agrees reasonably well with the expected increase $3.7 \times 10^{20} \text{ cm}^{-3}$ if 3% of V atoms are replaced by W.

The electron density mainly affects the bulk film property; photocurrent performance is also affected by the properties of the photoanode surface. In order to gain a clear understanding of the observed enhancement, the light absorption efficiency, charge separation efficiency in the bulk of the film, and interfacial charge transfer efficiency are determined and analyzed next.

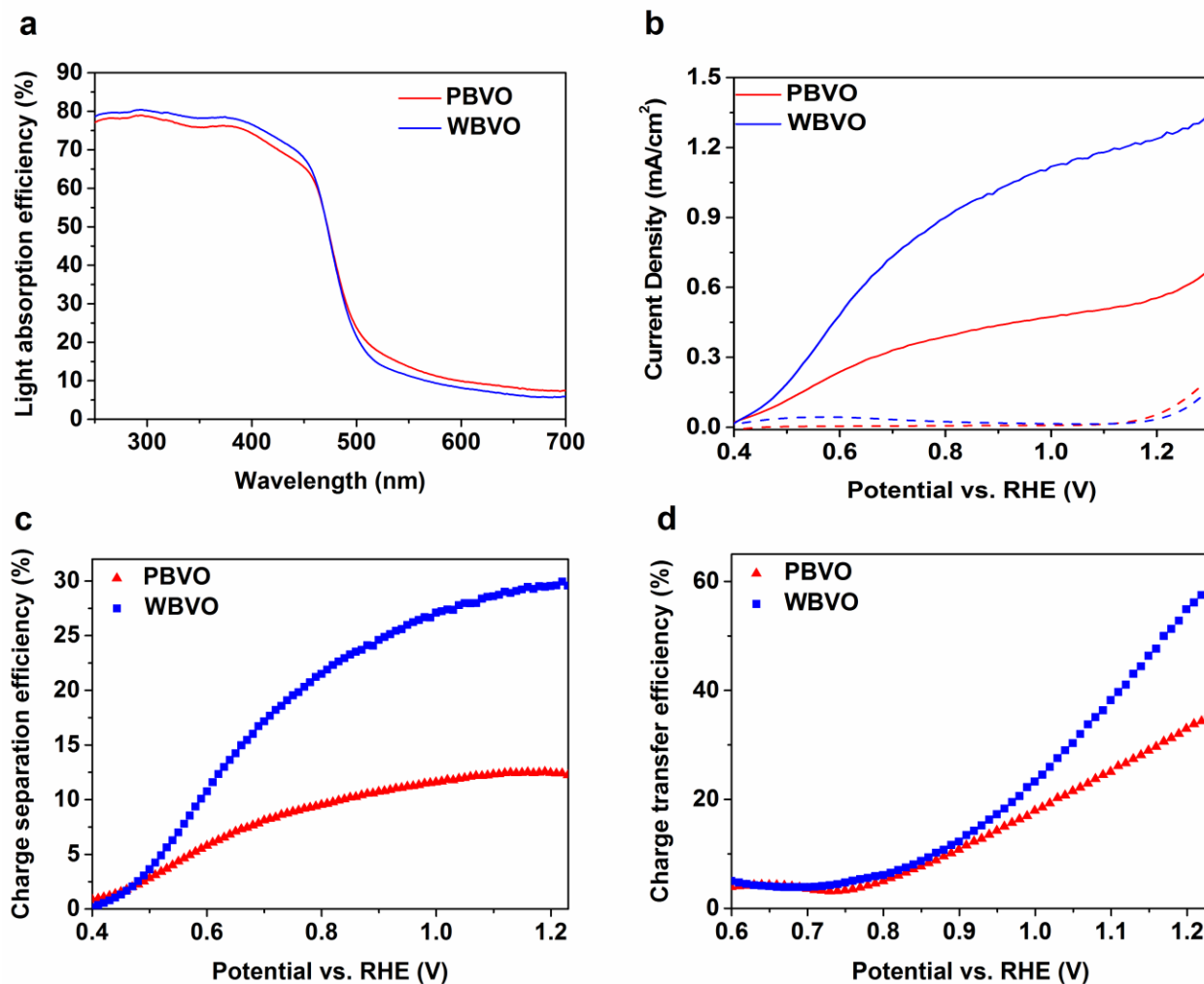


Fig. 3 (a) Light absorption efficiency, (b) oxidation photocurrents in electrolyte with hole scavenger Na_2SO_3 , (c) charge separation efficiency and (d) charge transfer efficiency of PBVO and WBVO.

The water oxidation photocurrent $J_{\text{H}_2\text{O}}$ is contributed by the three efficiencies, light absorption efficiency (η_{abs}), charge separation efficiency in the bulk of the film (η_{sep}), and interfacial charge transfer efficiency (η_{tran}):²⁸

$$J_{\text{H}_2\text{O}} = J_0 \times \eta_{\text{abs}} \times \eta_{\text{sep}} \times \eta_{\text{tran}} = J_{\text{abs}} \times \eta_{\text{sep}} \times \eta_{\text{tran}} \quad (2)$$

where J_0 is the theoretical solar photocurrent which assumes that all the solar energy corresponding to the band edge can be fully converted to fuel energy (7.3 mA/cm² for BiVO_4).⁹ In order to quantitatively analyze the contribution, an effective hole scavenger Na_2SO_3 is utilized to suppress the surface charge recombination due to the slow oxidation kinetics. In the presence of hole scavenger Na_2SO_3 , the charge transfer efficiency can be approximated to be 100% ($\eta_{\text{inj}}=1$) due to the fast oxidation kinetics of Na_2SO_3 .²⁸ Under this approximation, the Na_2SO_3 oxidation photocurrent is determined by:²⁸

$$J_{\text{Na}_2\text{SO}_3} = J_0 \times \eta_{\text{abs}} \times \eta_{\text{sep}} = J_{\text{abs}} \times \eta_{\text{sep}} \quad (3)$$

where $J_{\text{Na}_2\text{SO}_3}$ is the oxidation photocurrent using Na_2SO_3 . From equations (2) and (3), we can obtain the charge separation efficiency $\eta_{\text{sep}}=J_{\text{Na}_2\text{SO}_3}/J_{\text{abs}}$ and the charge transfer efficiency $\eta_{\text{tran}}=J_{\text{H}_2\text{O}}/J_{\text{Na}_2\text{SO}_3}$. To begin with the quantitative analysis, light absorption efficiencies of PBVO and WBVO have to be measured. As shown in Fig. 3a, there is not much difference in the light absorption efficiencies of PBVO and WBVO. According to the light absorption efficiencies, J_{abs} is calculated to be 4.01 mA/cm² and 4.07 mA/cm² for PBVO and WBVO, respectively. And the Na_2SO_3 oxidation photocurrent is also measured as shown in Fig. 3b.

The calculated charge separation efficiency of PBVO is about 12% at 1.23 V vs. RHE, whereas that of WBVO is about 30% (Fig. 3c). The charge transfer efficiency of PBVO is about 34% at

1.23 V vs. RHE, and that of WBVO is about 60% (Fig. 3d). As a result, the observed enhancement in photocurrent is contributed by both increased charge separation and charge transfer. The enhanced bulk charge separation is from the enhanced electron density as discussed above. However, further analysis is needed to understand how the W doping has affected the surface charge transfer.

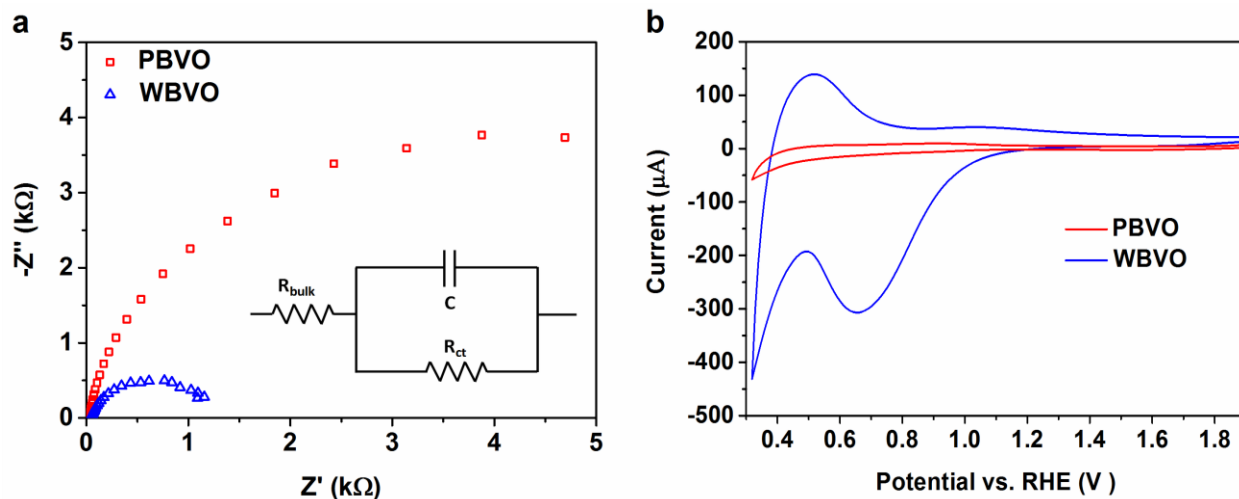


Fig. 4 (a) Electrochemical impedance spectra (EIS) of PBVO and WBVO measured at the applied potential of 1.23 V vs. RHE in 0.5M Na₂SO₄ electrolyte under 1 sun solar simulator illumination. The inset in Fig. 4a is the equivalent circuit to simulate the EIS. R_{bulk} represents total resistance from external circuit; C is the bulk capacitance; R_{ct} is charge transfer resistance of holes from PBVO or WBVO surface to water. (b) Cyclic voltammetry scan of PBVO and WBVO in the dark at a scan rate of 100 mV s⁻¹ after holding the electrode at the potential of 1.8 V vs. RHE for 120 seconds under 1 sun illumination.

In order to unravel the root cause of the enhanced surface charge transfer efficiency by W doping, EIS has been taken. To reflect the actual situation of the surface reactions during water oxidation, EIS was performed under solar illumination. Fig. 4a shows the Nyquist plots, in which the radius of the semicircle for the sample PBVO is larger than that of WBVO, indicating a larger surface resistance PBVO. According to previous work, an equivalent circuit is employed to analyze the surface charge transfer (inset in Fig. 4a).²⁹ In the equivalent circuit, R_s represents the resistances of the FTO film, the external

electrical contacts and the liquid electrolyte, C is the bulk capacitance, R_{ct} (charge transfer resistance) represent the resistance of charge transfer at the semiconductor/electrolyte interface. The fitting results show that R_s values are around $35\ \Omega$ for both PBVO and WBVO. The surface charge transfer resistance, R_{ct} , of PBVO is about $6945\ \Omega$, while that of WBVO is much smaller at around $1041\ \Omega$. This result indicates that W doping can lower the surface charge transfer resistance, which is consistent with the observed charge transfer efficiency enhancement. To unravel how W doping affects the charge transfer, the surface condition in the BiVO_4 is critical.

It is known that hydroxyterminated surface states will be formed on metal oxide electrode surface in aqueous solution.³⁰⁻³² According to a previous report, the surface states will be charged by holes prior to the water oxidation.³³ These active surface states can be characterized by reduction cyclic voltammetry scan, in which current peaks can be revealed due to the reduction of those charged surface species.³³ In this study, we employed this technique to investigate the surface condition by W doping. As shown in Fig. 4b, we carried out cyclic voltammetry scan of BiVO_4 in Na_2SO_4 electrolyte at a scan rate of $100\ \text{mV}\cdot\text{s}^{-1}$ after holding the electrode at the potential of $1.8\ \text{V}$ vs. RHE for 120 seconds under 1 sun illumination. It shows that for PBVO, no obvious reduction peak has been observed, while one obvious reduction peak around $0.7\ \text{V}$ vs. RHE is seen for WBVO. It is thus concluded that W doping has introduced an active surface state participating in the water oxidation. This observation also explains why the W doped BiVO_4 has a lower charge transfer resistance contributing to the higher transfer efficiency.

3.2 Theoretical calculations

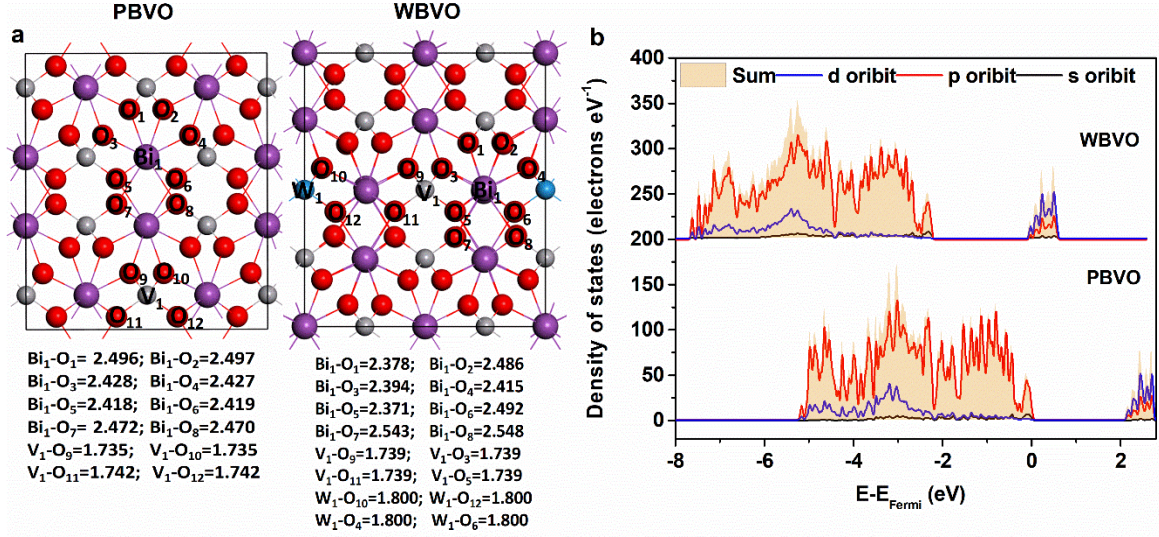


Fig. 5 (a) Crystal Structure of PBVO and WBVO. Bi, V, O, W atoms are represented by purple, grey, red, and blue colours. (b) Density of States (DOS) of PBVO and WBVO.

The $2 \times 1 \times 2$ supercell model of PBVO and WBVO are shown in Fig. 5a. Monoclinic BiVO_4 is composed of a layered structure along the crystallographic c axis (Fig. 5a), in which two polyhedra units, VO_4 tetrahedra and BiO_8 dodecahedra links to each other by edge sharing.²⁵ In WBVO, the doping element, W, substitutes V, and is displayed in blue color (Fig. 5a). Considering the possibility of interstitial substitution, the defect formation energy was calculated (Table S2) for the two different interstitial sites (Fig. S2).³⁴ The formation energy shows that interstitial W is unlikely to happen due to its high formation energy. Thus, here we only calculated the defect formation energy of W replacing V. As seen from Fig. 5a, the substitution of V causes slight deformation of the structure. The bond length of Bi-O (NO. 1-5) shows a small decrease, while that of Bi-O (NO. 6-8) shows a slight increase. However, there is no much difference in the V-O bond length. The bond length W-O is generally a little larger than that of the substituted V-O, which is mainly due to the larger ionic radius of W (0.6 Å) than V (0.54 Å). Fig. 5b shows the DOS of PBVO and WBVO. The valence band (VB) and conduction band (CB) are mainly composed of O 2p states and V 3d states. The Bi 6p and 6s states also contribute to the composition of VB and CB. Compared with PBVO, one feature is the formation of a localized filled state inside the bandgap, which is composed of O 2p and V 3d states. Such kind of localized state usually

serves as recombination centers. The finding of the localized state helps explain the reported performance increase at a small doping concentration and then decrease at a higher doping concentration.³⁵ The localized state assists the charge separation through increased the majority charge carrier concentration on the one hand, and promotes charge recombination on the other hand. Therefore, an optimized doping concentration is critical to achieve a balance between charge concentration and charge recombination.

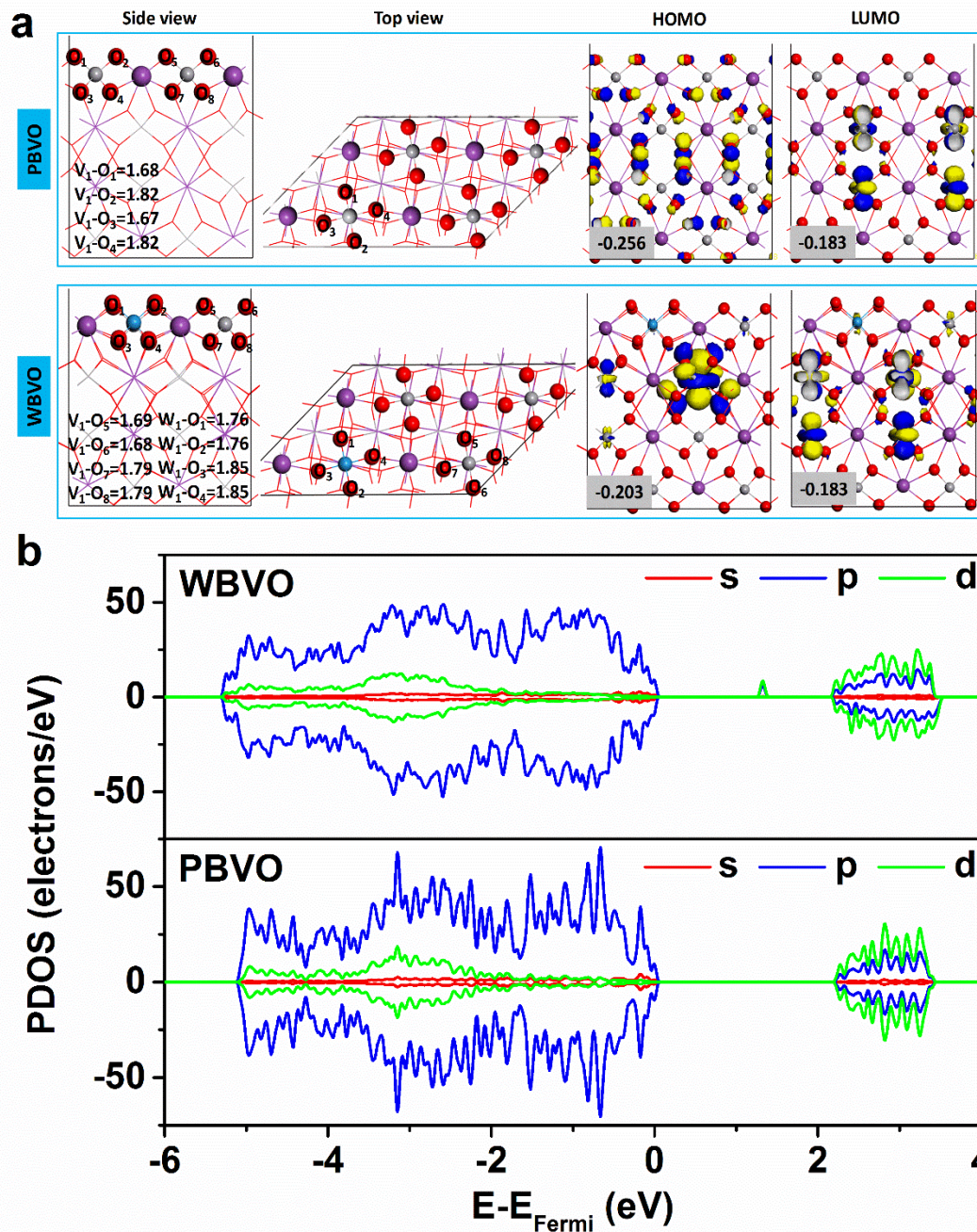


Fig. 6 (a) Side view and top view of PBVO and WBVO (010) facet. (b) The corresponding partial density of states (PDOS) of PBVO and WBVO (010) facets.

The optimized PBVO and WBVO (010) facet are shown in Fig. 6a. As seen from Fig. 6a-b, the substitution of V by W causes some deformation around the substitution site, around which the well overlapped O atoms (red spheres) in the PBVO are now separated and can be distinguished in WBVO.

The bond length has also changed. From the PDOS of PBVO and WBVO (010) facets (Fig. 6b), a filled state inside the bandgap is observed, which is contributed by V 3d and O 2p orbitals. The spin-up ($y>0$) and spin-down ($y<0$) DOS are the same for PBVO. However, for WBVO, there is substantial difference between the spin-up and spin-down PDOS. The symmetry of the spin-up and spin-down PDOS is related to the polarization of spin moment of transition metal (V atom).³⁶ The un-symmetric spin state (polarized state) PDOS inside the bandgap suggests the absence of surface V atoms in certain spin direction, and such surface termination influences the adjacent O atoms to become polarized too.³⁶ Thus, the observed filled state inside the bandgap is mainly composed of V 3d and O 2p orbitals. In the experiment (Fig. 4b), an active surface state was observed. Combined with the theoretical analysis, the observed active surface state is likely to be surface V site, since charge distribute on surface V sites and a surface filled state (from PDOS) is also contributed by V 3d orbitals. The spin density map of W-doped BiVO₄ shows the localization of an electron on V (Fig. S1).

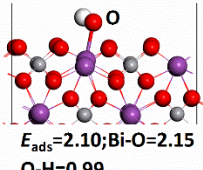
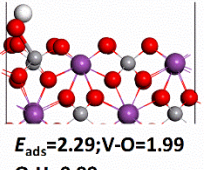
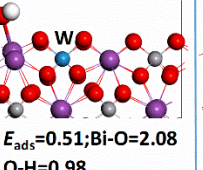
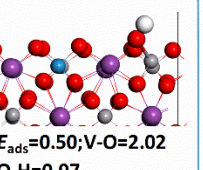
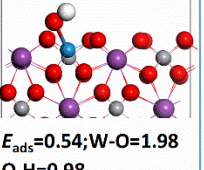
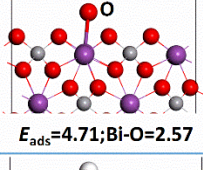
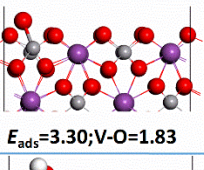
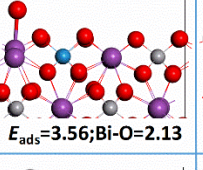
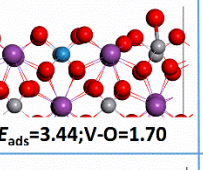
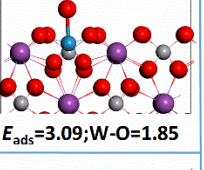
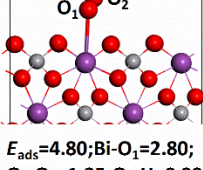
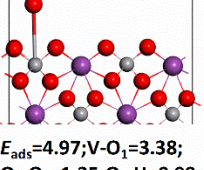
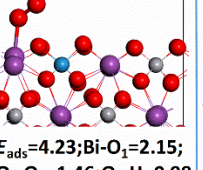
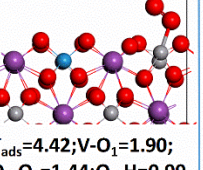
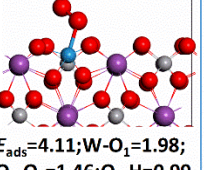
| | PBVO | | WBVO | | |
|----------------------|--|---|--|--|---|
| | Bi site | V site | Bi site | V site | W site |
| @ OH _{ads} |  $E_{ads}=2.10$; Bi-O=2.15 O-H=0.99 |  $E_{ads}=2.29$; V-O=1.99 O-H=0.99 |  $E_{ads}=0.51$; Bi-O=2.08 O-H=0.98 |  $E_{ads}=0.50$; V-O=2.02 O-H=0.97 |  $E_{ads}=0.54$; W-O=1.98 O-H=0.98 |
| @ O _{ads} |  $E_{ads}=4.71$; Bi-O=2.57 |  $E_{ads}=3.30$; V-O=1.83 |  $E_{ads}=3.56$; Bi-O=2.13 |  $E_{ads}=3.44$; V-O=1.70 |  $E_{ads}=3.09$; W-O=1.85 |
| @ OOH _{ads} |  $E_{ads}=4.80$; Bi-O ₁ =2.80; O ₁ -O ₂ =1.35; O ₂ -H=0.99 |  $E_{ads}=4.97$; V-O ₁ =3.38; O ₁ -O ₂ =1.35; O ₂ -H=0.99 |  $E_{ads}=4.23$; Bi-O ₁ =2.15; O ₁ -O ₂ =1.46; O ₂ -H=0.98 |  $E_{ads}=4.42$; V-O ₁ =1.90; O ₁ -O ₂ =1.44; O ₂ -H=0.99 |  $E_{ads}=4.11$; W-O ₁ =1.98; O ₁ -O ₂ =1.46; O ₂ -H=0.99 |

Fig. 7 Adsorption structures and energies of OH_{ads}, O_{ads} and OOH_{ads} involved in a water splitting process on PBVO and WBVO (010) facet. The “-” and “@” signs stand for bond and adsorption state on the facet, respectively.

Fig. 7 displays the adsorption of several key species involved in the water oxidation on BiVO₄ (010) facet with and without W doping. The adsorption energies of OH_{ads} on Bi and V atoms of the (010) facet of WBVO are much smaller (0.5-0.51 eV) than those of PBVO (2.1-2.29 eV). In addition, the adsorption energy of OH_{ads} on the substitution site (W atom) also has a similar value with that of V. This indicates W doping greatly favors the adsorption of OH_{ads}. For O_{ads}, the adsorption energy on Bi atom of WBVO decreases, while on V atom the adsorption energy shows a slight increase. However, the substitution site W shows a decreased adsorption energy. Thus, W doping shows a favorable adsorption of O_{ads} on Bi and W atom sites. For OOH_{ads}, the adsorption energy on Bi and V atoms of WBVO also decreases, indicating a better adsorption properties of OOH_{ads} after W doping. Moreover, the bond lengths between surface atoms (Bi, V or W) and adsorption species (OH_{ads}, O_{ads} and OOH_{ads}) become smaller after introducing W doping, especially for the adsorption of OOH_{ads} on V atom, which indicates that W doping facilitates the adsorption of these species. The comparison of adsorption of surface species involved in the water oxidation clearly indicates that W doping favors the surface catalysis process.

4. Discussion

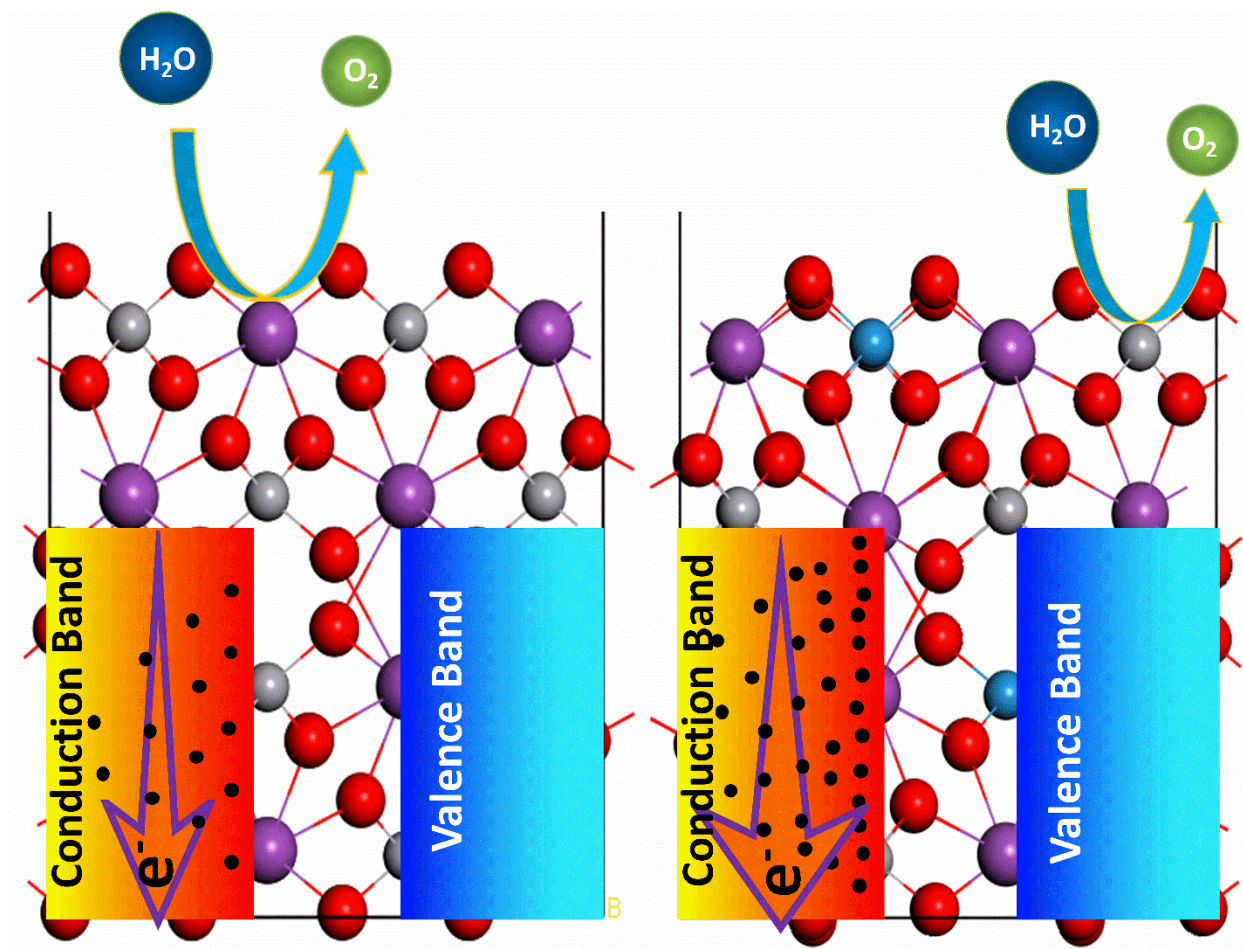


Fig. 8 Schematic description of the PEC water splitting process on BiVO_4 with or without W doping.

Based on the above analyses, the mechanism of the effect of W doping on the performance of BiVO_4 photoanode for PEC water splitting performance is proposed, as shown in Fig. 8. For the bulk charge separation, W doping greatly enhances the electron density and results in a better electron separation. For the surface catalysis, W doping greatly influences the adsorption of several key species on BiVO_4 (010) facet, and plays a key role in enhancing the hole transfer for water oxidation. For pristine BiVO_4 , surface holes are dispersed on Bi atoms, and no specific active sites can be distinguished as efficient oxidation sites. However, W doping activates the V atoms to be active reaction sites, which favors in the adsorption of key species involved in water oxidation. The PDOS also indicates V contributes to the surface filled state. From experimental observation, an active surface state has been found after W doping, which is consistent with the theoretical calculation. It is reasonable to deduce that the active surface state is the

surface V site, which functions as charge transfer center. In addition, the bond lengths between surface atoms (Bi, V or W) and adsorption species (OH_{ads} , O_{ads} and OOH_{ads}) become smaller after W doping. The prediction from theoretical calculations is consistent with the observation of active surface states and the lower hole transfer resistance found in experiment. Thus, an enhanced surface hole transfer efficiency has been observed after W doping into BiVO_4 .

5. Conclusion

Planar structured BiVO_4 thin films with and without W doping has been successfully prepared. W doping has not changed the morphology and crystallinity of the films. However, W doping has enhanced the photocurrent significantly. The enhancement mainly comes from better charge separation and enhanced surface charge transfer. The better charge separation is due to the improved carrier density caused by the doping. W doping also lowers the surface charge transfer resistance and forms active surface states facilitating the charge transfer. Theoretical analysis shows that W doping has changed the reactive surface sites from Bi atom to V atom. W doping also facilitates the adsorption of the OH_{ads} , O_{ads} and OOH_{ads} involved in a water splitting process. In addition, the bond lengths between surface atoms (Bi, V or W) and adsorption species (OH_{ads} , O_{ads} and OOH_{ads}) are shortened after W doping. Current study provides important insights into the roles of W doping in BiVO_4 , especially on the surface catalysis.

Acknowledgements

‡ These two authors contributed equally to this work.

Financial supports from Ministry of Education (grant RG15/16). Financial supports from Nanyang Technological University in form of SUG. Singapore National Research Foundation through the Singapore-Berkeley Initiative for Sustainable Energy (SINBERISE) CREATE Programme. Financial supports from the National Natural Science Foundation of China (No. 21676216)

References

1. M. G. Walter, E. L. Warren, J. R. McKone, S. W. Boettcher, Q. Mi, E. A. Santori and N. S. Lewis, *Chem. Rev.*, 2010, **110**, 6446-6473.
2. Z. Li, W. Luo, M. Zhang, J. Feng and Z. Zou, *Energy Environ. Sci.*, 2013, **6**, 347-370.
3. M. Grätzel, *Nature*, 2001, **414**, 338-344.
4. P. M. Rao, L. Cai, C. Liu, I. S. Cho, C. H. Lee, J. M. Weisse, P. Yang and X. Zheng, *Nano Lett.*, 2014, **14**, 1099-1105.
5. Z. Li, J. Feng, S. Yan and Z. Zou, *Nano Today*, 2015, **10**, 468-486.
6. W. Luo, Z. Yang, Z. Li, J. Zhang, J. Liu, Z. Zhao, Z. Wang, S. Yan, T. Yu and Z. Zou, *Energy Environ. Sci.*, 2011, **4**, 4046-4051.
7. T. W. Kim, Y. Ping, G. A. Galli and K.-S. Choi, *Nat. Commun.*, 2015, **6**, 8769
8. W. Luo, Z. Li, T. Yu and Z. Zou, *J. Phys. Chem. C*, 2012, **116**, 5076-5081.
9. X. Zhao, W. Luo, J. Feng, M. Li, Z. Li, T. Yu and Z. Zou, *Adv. Energy Mater.*, 2014, **4**, 1301785.
10. K. J. McDonald and K.-S. Choi, *Energy Environ. Sci.*, 2012, **5**, 8553-8557.
11. F. F. Abdi, N. Firet and R. van de Krol, *ChemCatChem*, 2013, **5**, 490-496.
12. D. K. Lee and K.-S. Choi, *Nat. Energy*, 2018, **3**, 53-60
13. W. Luo, J. Wang, X. Zhao, Z. Zhao, Z. Li and Z. Zou, *Phys. Chem. Chem. Phys.*, 2013, **15**, 1006-1013.
14. J. Hu, X. Zhao, W. Chen, H. Su and Z. Chen, *J. Phys. Chem. C*, 2017, **121**, 18702-18709.
15. A. J. Rettie, H. C. Lee, L. G. Marshall, J.-F. Lin, C. Capan, J. Lindemuth, J. S. McCloy, J. Zhou, A. J. Bard and C. B. Mullins, *J. Am. Chem. Soc.*, 2013, **135**, 11389-11396.
16. R. Li, F. Zhang, D. Wang, J. Yang, M. Li, J. Zhu, X. Zhou, H. Han and C. Li, *Nature Commun.*, 2013, **4**, 1432.
17. J. Hu, W. Chen, X. Zhao, H. Su and Z. Chen, *ACS Appl. Mater. Interfaces*, 2018, **10**, 5475-5484.
18. X. Yao, D. Wang, X. Zhao, S. Ma, P. S. Bassi, G. Yang, W. Chen, Z. Chen, T. Sritharan, *Energy Technol.* **2017**, **6**, 100 –109.
19. T. W. Kim and K.-S. Choi, *Science*, 2014, **343**, 990-994.
20. M. Liao, J. Feng, W. Luo, Z. Wang, J. Zhang, Z. Li, T. Yu and Z. Zou, *Adv. Funct. Mater.*, 2012, **22**, 3066-3074.
21. G. Xu, Z. Xu, Z. Shi, L. Pei, S. Yan, Z. Gu, Z. Zou, *ChemSusChem*, 2017, **10**, 2897-2903.
22. F. F. Abdi, L. Han, A. H. Smets, M. Zeman, B. Dam and R. van de Krol, *Nature Commun.*, 2013, **4**, 2195
23. X. Zhao and Z. Chen, *Beilstein J. Nanotechnol.*, 2017, **8**, 2640-2647.
24. J. Yang, D. Wang, X. Zhou and C. Li, *Chem. Eur. J.*, 2013, **19**, 1320-1326.

25. Z. Zhao, Z. Li and Z. Zou, *RSC Adv.*, 2011, **1**, 874-883.
26. W. Liu, W. Zheng and Q. Jiang, *Phy. Rev. B*, 2007, **75**, 235322.
27. B. Engels, P. Richard, K. Schroeder, S. Blügel, P. Ebert and K. Urban, *Phy. Rev. B*, 1998, **58**, 7799.
28. H. Dotan, K. Sivula, M. Grätzel, A. Rothschild and S. C. Warren, *Energy Environ. Sci.*, 2011, **4**, 958-964.
29. S. Hernández, S. M. Thalluri, A. Sacco, S. Bensaid, G. Saracco and N. Russo, *Appl. Catal. A*, 2015, **504**, 266-271.
30. P. Salvador, *J. Electrochem. Soc.*, 1981, **128**, 1895-1900.
31. B. Klahr, S. Gimenez, F. Fabregat-Santiago, T. Hamann and J. Bisquert, *J. Am. Chem. Soc.*, 2012, **134**, 4294-4302.
32. B. E. Conway and B. V. Tilak, in *Advances in Catalysis*, eds. H. P. D.D. Eley and B. W. Paul, Academic Press, 1992, **38**, 1-147.
33. B. Klahr, S. Gimenez, F. Fabregat-Santiago, J. Bisquert and T. W. Hamann, *Energy Environ. Sci.*, 2012, **5**, 7626-7636.
34. V. Kulish, W. Liu, F. Benistant and S. Manzhos, *J. Mater. Res.*, 2018, **33**, 401-413.
35. S. P. Berglund, A. J. Rettie, S. Hoang and C. B. Mullins, *Phys. Chem. Chem. Phys.*, 2012, **14**, 7065-7075.
36. Y. Chen, E. Bylaska and J. Weare, *First principles estimation of geochemically important transition metal oxide properties. In: Molecular Modeling of Geochemical Reactions: An Introduction*, John Wiley & Sons, Ltd, 2016, pp. 107-149.